

XMM-Newton observations of the Galactic globular clusters NGC 2808 and NGC 4372

M. Servillat¹, N. A. Webb¹, and D. Barret¹

CESR, Université Paul Sabatier, CNRS – 9 avenue du Colonel Roche, 31400 Toulouse, France
e-mail: mathieu.servillat@cesr.fr

Received 20 July 2007 / Accepted 28 November 2007

ABSTRACT

Aims. Galactic globular clusters harbour binary systems that are detected as faint X-ray sources. These close binaries are thought to play an important role in the stability of the clusters by liberating energy and delaying the inevitable core collapse of globular clusters. The inventory of close binaries and their identification is therefore essential.

Methods. We present XMM-Newton observations of two Galactic globular clusters: NGC 2808 and NGC 4372. We use X-ray spectral and variability analysis combined with ultra-violet observations made with the XMM-Newton optical monitor and published data from the Hubble Space Telescope to identify sources associated with the clusters. We compare the results of our observations with estimates from population synthesis models.

Results. Five sources out of 96 are likely to be related to NGC 2808. Nine sources are found in the field of view of NGC 4372, none being located inside its half-mass radius. We find one quiescent neutron star low mass X-ray binary candidate in the core of NGC 2808, and propose that the majority of the central sources in NGC 2808 are cataclysmic variables. An estimation leads to 20 ± 10 cataclysmic variables with luminosity above 4.25×10^{31} erg s⁻¹. Millisecond pulsars could also be present in the core of NGC 2808, and some sources outside the half-mass radius could possibly be linked to the cluster.

Key words. Galaxy: globular clusters: individual: NGC 2808, NGC 4372 – X-rays: general – Stars: binaries: close

1. Introduction

XMM-Newton and Chandra X-ray observatories are currently revealing more and more faint X-ray sources in globular clusters (GCs) thanks to their high sensitivity and high angular resolution respectively (e.g. Webb et al. 2004, 2006; Heinke et al. 2003b, 2006). Thirteen bright X-ray sources with $L_X > 10^{36}$ erg s⁻¹ are found in the 152 known Galactic GCs. These are neutron star low-mass X-ray binaries (LMXBs) showing type I X-ray bursts (e.g. Lewin & Joss 1983). Numerous faint X-ray sources with $L_X < 10^{34.5}$ erg s⁻¹ have been shown to be a variety of objects, mainly binaries such as LMXBs in quiescence (qLMXBs), cataclysmic variables (CVs), active binaries (ABs), or millisecond pulsars (MSPs), the probable progeny of LMXBs. These objects have been classified through multi-wavelength analysis: qLMXBs are usually identified by their soft blackbody-like X-ray spectra (e.g. Gendre et al. 2003a,b), CVs can be confirmed by their blue, variable optical counterpart (e.g. Webb et al. 2004), ABs by their main-sequence, variable optical counterparts (e.g. Edmonds et al. 2003), and MSPs by their radio counterpart (e.g. Grindlay et al. 2001).

It is clear that through mass segregation, heavy objects such as binaries are concentrated towards the core of GCs (Lightman & Grindlay 1982). Therefore, we expect the majority of X-ray binaries, which are more massive than the mean stellar mass, to be located inside the half-mass radius. Hurley et al. (2007) showed from simulations that the fraction of primordial binaries destroyed in the core by a variety of processes is balanced by the combination of mass-segregation and creation of new binaries in exchange interactions, leading to a marked increase of the binary fraction in the central regions. Outside the half-mass radius, the primordial binary fraction is well pre-

served (Hurley et al. 2007) which could explain the presence of close binaries located outside of the half-mass radius, as a CV in M 22 (Pietrukowicz et al. 2005). D’Amico et al. (2002) and Colpi et al. (2003) also discussed the case of two MSPs outside the half-mass radius of NGC 6752 which could have been ejected from the GC through interactions with a central massive object.

From early X-ray observations of GCs, we know that they are efficient at producing X-ray binaries in their core compared to the field. Using the eleven known bright LMXBs in GCs (now thirteen), Verbunt & Hut (1987) showed that LMXBs in GCs are produced dynamically through exchange encounters of isolated neutron stars with primordial binaries as opposed to the much less probable evolution of a primordial binary into an LMXB. Observations also support the fact that qLMXBs in GCs scale with the cluster encounter rate (Gendre et al. 2003a; Pooley et al. 2003), implying that qLMXBs are formed through dynamical processes which occur in dense stellar systems. Concerning CVs, following their discovery in significant numbers in 47 Tuc (Grindlay et al. 2001), it has been pointed out following population synthesis studies (Ivanova et al. 2006; Trenti et al. 2007) and from observations (e.g. Webb et al. 2004; Pooley & Hut 2006) that they may be formed in GCs either dynamically or, for a lower fraction, from primordial binaries.

Neglecting the role of binaries, we know that GC evolution leads to a core collapse followed by the GC disruption on a timescale shorter than the mean age of GCs, estimated to be 11.5 ± 2.6 Gyr (Carretta et al. 2000). This core collapse must have been delayed by an internal energy source to explain the GC longevity, and binaries could play this role (see Hut et al. 1992, 2003, for a review). In the core, binaries are subject to en-

Table 1. Globular cluster parameters from Harris (1996, updated Feb. 2003)

Parameters	NGC 2808	NGC 4372
Right Ascension (J2000)	9 ^h 12 ^m 02.6 ^s	12 ^h 25 ^m 45.4 ^s
Declination (J2000)	-64°51'47"	-72°39'33"
Distance [kpc]	9.6	5.8
Core radius, r_c [']	0.26	1.75
Half mass radius, r_h [']	0.76	3.90
Tidal radius, r_t [']	15.55	34.82
r_c/r_h	0.34	0.45
Half-mass relaxation time [yr]	1.35×10^9	3.89×10^9
Mass ^a [M_\odot]	1.46×10^6	3.08×10^5
Metallicity, [Fe/H]	-1.15	-2.09

^a calculated from the relation $M/M_\odot = 3 \times 10^{0.4(M_v^\odot - M_v)}$ using the absolute visual magnitude.

counters and hard binaries become harder while transferring their energy to passing stars. This scenario leads to a global heating of the core, and even a small population of close binaries can drive the evolution of the entire cluster (Hut et al. 1992). Some GCs could also contain an intermediate mass black hole (IMBH) of $\sim 10^3 M_\odot$ or more in their core to explain the distribution of stars in some clusters, and the stability on large time scales. The presence of an IMBH was claimed for M 15 (Gerssen et al. 2002, see also Ho et al. 2003), for G1 in the galaxy M 31 (Gebhardt et al. 2002, 2005), and for extragalactic GCs hosting an ultra luminous X-ray source (Maccarone et al. 2007).

The targets studied in this paper are two very different GCs. NGC 2808 is a massive and concentrated cluster. NGC 4372 on the contrary is less dense with fewer stars, being also a very low metallicity cluster. Their parameters are listed in Table 1.

NGC 2808 has already been studied in X-rays with the GIS instrument on board ASCA observatory. Only one source was reported in the GIS catalogue (Ueda et al. 2001) with a 1.35' error circle located at 7.5' from the cluster center. No sources were reported during the ROSAT All Sky Survey observations (Voges et al. 1999). The core of NGC 2808 was also observed with the Space Telescope Imaging Spectrograph (STIS) on board the Hubble Space Telescope (HST) in 2000 with ultra-violet (UV) filters F25QTZ (far-UV band centered at 159 nm) and F25CN270 (near-UV band centered at 270 nm). Dieball et al. (2005) looked for white dwarfs (WDs) and CVs in this data. They found ~ 40 WD and ~ 60 CV candidates in the field of view. Two of the CV candidates are variable (UV 222 and UV 397), and another has an optical counterpart (UV 170). NGC 2808 has also been observed in detail in the optical, and since Harris (1974), it has been known that the horizontal branch in NGC 2808 is unusual (see also Bedin et al. 2000; Carretta et al. 2006). The main sequence is separated into three branches, possibly due to successive rounds of star formation, with different helium abundances (Piotto et al. 2007).

In the optical, the colour-magnitude diagram of NGC 4372 indicates an old cluster (15 ± 4 Gyr), with high reddening, but no special features (Alcaino et al. 1991). Kaluzny & Krzeminski (1993) found 19 variable stars, of which one has a light curve consistent with an eclipsing CV of period 0.4 days. In the X-ray, the ROSAT Observatory, with the HRI instrument, detected 19 sources (Johnston et al. 1996), of which 9 fall in our field of view. All these sources are located outside of the half-mass radius of the cluster, and none are consistent with the variable stars detected in the optical.

2. X-ray observations and data processing

NGC 2808 was observed on February 1st 2005, for 41.8 kiloseconds (ks) with the three European Photon Imaging Cameras (EPIC MOS1, MOS2 and pn) on board the XMM-Newton observatory, in imaging mode, using a full frame window and a medium filter.

The observation of NGC 4372 was performed under the same conditions on March 23–24th 2005, for 29.7 ks, but the MOS1 CCD6 was inoperative (micro-meteorite event on March 9th 2005), and the pn data was lost due to technical issues.

2.1. Data reduction and filtering

We processed the data using the XMM-Newton Science Analysis System v7.0 (SAS). We used the *emproc* and *epproc* scripts with the most recent calibration data files to reduce the EPIC observation data files (ODFs). During this step, bad events mostly due to bad rows, edge effects, and cosmic ray events were flagged. We filtered the three resulting event lists for event patterns in order to maximise the signal-to-noise ratio against non X-ray events. We selected only calibrated patterns, i.e. simple and double events for pn data and single to quadruple events for MOS data. For pn events below 500 eV, we selected only single events because in this energy band non X-ray events also affect double events (Ehle et al. 2006, §3.3.7).

Based on the light curve of single events exceeding 10 keV we identified periods of high background, due to soft proton flares, and selected good time intervals for the observation. For NGC 2808, this operation leads to 38.0, 37.3 and 30.2 ks of clean observation for MOS1, MOS2 and pn respectively. For NGC 4372, the observation was highly affected by flares and only 15.7 ks for MOS1 and 17.2 ks for MOS2 remain after filtering. We note that flaring activity is continuous during the exposure and events with energy above 2 keV are affected by a high noise, even after filtering.

2.2. Source detection

The list of events was divided into three energy bands (0.5–1.5, 1.5–3, and 3–10 keV) to allow us to derive spectral colours. The source detection was done for all available data simultaneously (MOS1, MOS2 and pn where available).

We performed the source detection using the script *edetect_chain* which first calculates the live time, the vignetting, the sensitivity map and the background map for each detector and each energy band, and then calls a sliding box algorithm. Finally we ran the task *emldetect*. For each source, the task performs a point spread function (PSF) fitting, for all the available detectors and for the three bands simultaneously, refines the coordinates, and gives the count rates, the hardness ratios, and the maximum likelihood (ML) of each source candidate.

The fluxes were obtained by providing the energy conversion factors (ECFs, in units of 10^{11} count $\text{cm}^2 \text{erg}^{-1}$) which allow the direct conversion of count rates into fluxes (flux = rate / ECF). These factors were calculated in each energy band and for each detector by extracting an on-axis source and generating detector response files for the source (using *rmfgen* and *arfgen* SAS tasks). These response files were used to create a fake spectrum corresponding to a common model: a power law spectrum with $\Gamma = 1.7$ (mean spectrum of detected sources) and the absorption (N_H) of the cluster. For NGC 2808, the absorption of $1.2 \times 10^{21} \text{cm}^{-2}$ was calculated from the reddening of optical observations (Bedin et al. 2000) with the relation computed by

Burstein & Heiles (1978). For NGC 4372, the reddening estimated by Alcaino et al. (1991) allows us to determine an absorption of $2.8 \times 10^{21} \text{ cm}^{-2}$. Finally, ECFs were calculated by dividing the count rates of the fake spectrum by the model fluxes. The obtained fluxes were then converted to unabsorbed fluxes. This method gives a reliable estimation of the ECFs we need for our energy bands. To give an idea of the errors on these values, by changing the spectral index of the model to $\Gamma = 2.0$, the fluxes changed by 1.5%, 2%, and 8%, in the energy bands 0.5–1.5, 1.5–3 and 3–10 keV respectively.

We processed the entire field of view with a spatial binning factor of 80, giving images with square pixels of side $4''$. This gives pixels of a similar size to the pn pixel size ($4.1'' \times 4.1''$), but larger than the MOS pixels ($1.1'' \times 1.1''$). The binning is sufficiently small to sample the PSF of the two detectors correctly, where the pn and MOS PSF FWHM (Full Width Half Maximum) are $6''$ and $5''$ respectively (Ehle et al. 2006, §3.1). We used a sliding box of 5×5 pixels to detect the sources, and selected sources with a ML greater than 10 (4σ detection).

For NGC 2808, this leads to the detection of 92 sources, all of which were visually verified for each detector. Five sources fall outside the pn detector, four for MOS1 and three others for MOS2. In the central region of the detectors, along the line of sight of the center of the GC, we noted that a source has a complex form. In this region, the PSF is narrower and better defined and the vignetting is the lowest. We therefore reprocessed the data with a spatial binning of 40 to get squared pixels of side $2''$ and thus better sample the PSF for MOS detectors. We listed from visual inspection eight possible sources, and used the task *emldetect* to simultaneously fit those source candidates. We detect five additional sources at a minimum of 4σ (C1 to C5) in the half mass radius of the cluster, of which 3 fall inside the core radius. Three others are detected at 2.5σ . We have a total number of 96 sources detected above 4σ . Their properties are listed in Table 2, the combined image is presented in Fig. 1, and a colour image, with a zoom of the center, in Fig. 2.

For NGC 4372, 10 sources were detected. Three sources were detected with the MOS2 only, in the region where the MOS1 CCD6 fell. None of these sources are located inside the half mass radius. The X-ray source properties are listed in Table 3, and the contour map is presented in Fig. 3.

3. Ultra-violet observations and data reduction

Along with the EPIC instruments, the Optical Monitor (OM) on board the XMM-Newton observatory performed three exposures of 4000 seconds for both NGC 2808 and NGC 4372 with the UVM2 filter, centered at 231 nm in the UV band. For this filter, the PSF FWHM is $1.8''$ and the field of view is approximately $16' \times 16'$.

The UV data was processed with the SAS task *omichain*. This script removes bad pixels, performs spatial calibration, and source detection for each image. For each source, the instrumental magnitude is evaluated from the count rate. Finally the resulting images and source lists are merged. We considered a significance threshold of 3σ for detected sources.

For NGC 2808, we detected 598 sources at a limiting UVM2 magnitude of 19.3. The region inside the half-mass radius is overcrowded and poorly resolved. Approximately 45 X-ray sources fall inside the OM field of view, for which we found nine matching UV sources. The properties of the UV counterparts are listed in Table 4. We took into account the X-ray position accuracy of the sources ($\sim 3.6''$, 90% error circles) and the UV position accuracy ($\sim 2.0''$, 90% error circles). We thus kept

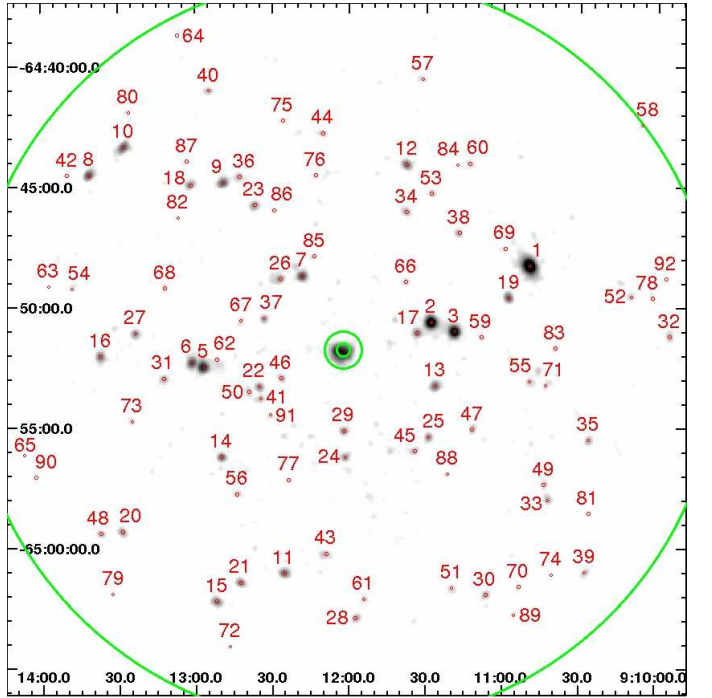


Fig. 1. Combined image of the XMM-Newton observation of NGC 2808. The three centered circles shown represent the core, half-mass and tidal radii. The detected sources are plotted with their 90% error circles. We used a spatial binning factor of 80 and the image was smoothed with a Gaussian filter. For this reason the core appears blurry, a zoom is shown in Fig. 2.

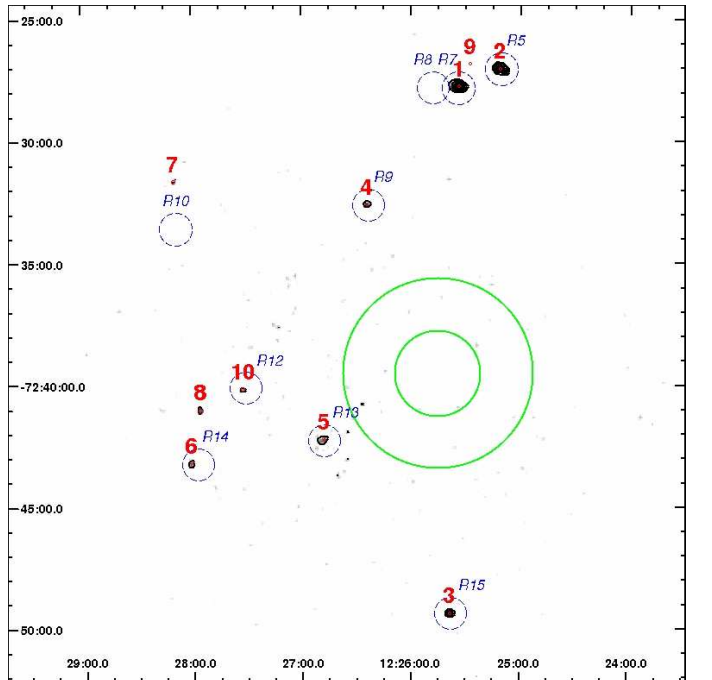


Fig. 3. Contour map of the XMM-Newton MOS2 observation of NGC 4372. Core and half-mass radii are shown. The detected sources are plotted with their 90% error circles and with contours at 3, 5 and 10σ . Small circles are XMM-Newton sources and bigger dashed circles are ROSAT sources with their error circle as reported by Johnston et al. (1996).

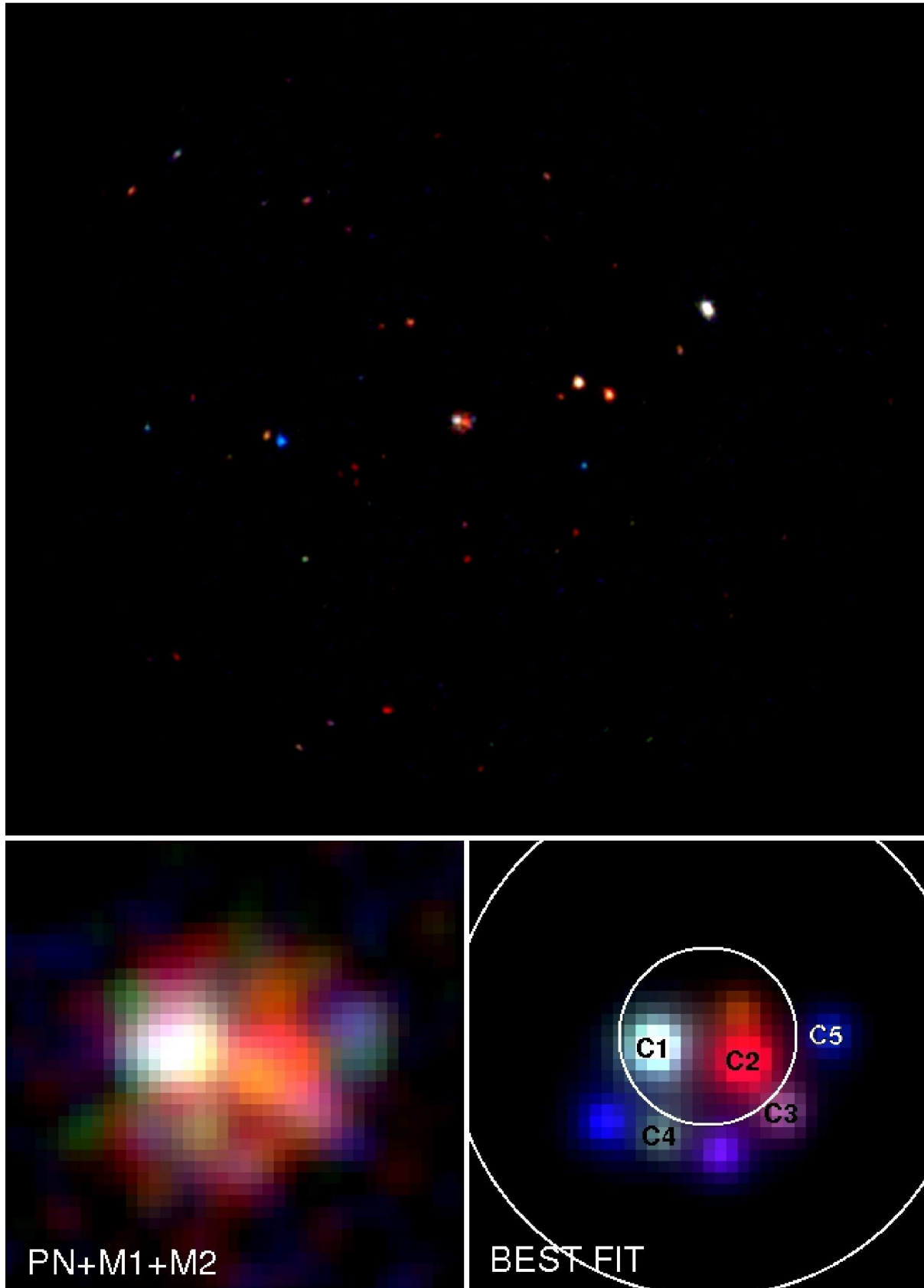


Fig. 2. *Top:* XMM-Newton observation of NGC 2808. Colours correspond to different energy bands, red: 0.5–1.5 keV, green: 1.5–3 keV, blue: 3–10 keV. The field of view is 30' across. The binning factor is 40 and the image was smoothed with a Gaussian filter. *Bottom:* A zoomed combined image of the three detectors is shown on the left and the image on the right shows a reconstruction of the core with eight sources (only five are detected at 4σ , the other three are detected at 2.5σ). The core and the half-mass radii are shown.

Table 4. List of UV counterparts in the NGC 2808 field of view. The X-ray source ID is given with the position of the UV source (90% error is $2.0''$), the offset position between UV and X-ray source, the offset from the cluster center, and the UVM2 magnitude.

ID	RA ₂₀₀₀	Dec ₂₀₀₀	Offset X-ray	Offset center	UVM2
1	09 ^h 10 ^m 49.9 ^s	-64°48'15.48"	1.18"	8.51'	18.40 ± 0.01
2	09 ^h 11 ^m 28.3 ^s	-64°50'36.60"	1.61"	3.85'	18.32 ± 0.01
17	09 ^h 11 ^m 33.6 ^s	-64°51'04.32"	0.54"	3.17'	10.95 ± 0.01
22	09 ^h 12 ^m 35.3 ^s	-64°53'19.32"	2.06"	3.77'	18.01 ± 0.01
24	09 ^h 12 ^m 01.7 ^s	-64°56'12.84"	1.69"	4.46'	14.80 ± 0.01
29	09 ^h 12 ^m 02.2 ^s	-64°55'10.56"	2.54"	3.35'	17.04 ± 0.01
50	09 ^h 12 ^m 02.2 ^s	-64°55'10.56"	2.52"	4.27'	18.97 ± 0.01
77	09 ^h 12 ^m 23.5 ^s	-64°57'11.88"	1.63"	5.84'	18.05 ± 0.01
85	09 ^h 12 ^m 13.7 ^s	-64°47'52.80"	1.24"	4.07'	17.24 ± 0.01

matching UV sources that have an offset with the X-ray source lower than $5.6''$. The X-ray sources with UV counterparts are all located outside the half-mass radius, and are therefore probably background or foreground sources.

We performed a Monte-Carlo simulation to evaluate the probability that the superposition of an X-ray source and a UV source occurred by chance. We excluded the central region inside a radius of $2.4'$ where the UV sources are not resolved. In the remaining area the X-ray and UV sources appeared to be uniformly distributed. The simulation leads to 1.1 ± 1.1 sources aligned fortuitously. We conclude that 8 ± 1 of the UV counterparts could be associated with their corresponding X-ray source with a probability of 99.9927%.

For NGC 4372, 272 sources were detected at a limiting UVM2 magnitude of 19.6. A bright A0 star in the field causes an out-of-focus ghost image (smoke ring) and lead to ~ 10 spurious detections. Only three X-ray sources fall in the region observed by the OM, and none has a UV counterpart.

4. The X-ray sources in NGC 2808

4.1. Members of NGC 2808

Most of the sources detected are background or foreground sources, but some of them are members of the cluster. If we assume no cosmic variance in the distribution of sources in the sky (see Yang et al. 2003), we can compare our observation with one without a GC to determine statistically the number of sources belonging to the cluster. We evaluated the number of background sources based on observations of the Lockman Hole (LH) with XMM-Newton. In this field, centered on the sky position RA₂₀₀₀ 10^h52^m43^s, Dec₂₀₀₀ +57°28'48", the absorption is very low, $N_H = 5.7 \times 10^{19} \text{ cm}^{-2}$ (Lockman et al. 1986).

We divided the XMM-Newton field of view into several annuli to take into account the vignetting, which becomes more important towards the edge of the field of view. The annuli are centered on the center of the GC, which is also the center of the sensitivity map of the detectors, and their size was chosen to encircle at least 5 detected sources, and when possible 20 sources. For each annulus, we evaluated the background count rate in several $15''$ radius regions without sources assuming a correction for the vignetting. A minimum detectable count rate was estimated to be equivalent to a ML of 10 above this background count rate. We assumed a power law spectrum with $\Gamma = 1.7$ with the absorption of the field of view, and entered the count rates into the

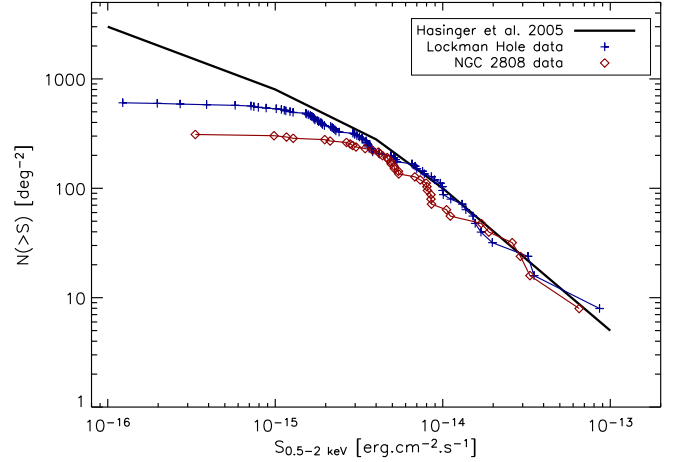


Fig. 4. $\log(N) - \log(S)$ diagram in the band 0.5–2 keV. S is the limiting flux and N the number of sources. The empirical relation of Hasinger et al. (2005) is reported for comparison.

tool WebPIMMS¹ v3.9b (Mukai 1993) to determine the minimum detectable unabsorbed flux of each annulus. In the center, this limiting flux is $F_{0.5-10 \text{ keV}} = 4.1 \times 10^{-15} \text{ erg cm}^{-2} \text{ s}^{-1}$, and goes up to $6.1 \times 10^{-15} \text{ erg cm}^{-2} \text{ s}^{-1}$ in the last annulus. This lead to a limiting luminosity of $L_{0.5-10 \text{ keV}} = 4.5 \times 10^{31} \text{ erg s}^{-1}$ for sources in the core of NGC 2808.

We used the $\log(N) - \log(S)$ relation derived by Hasinger et al. (2005) from a deep observation of the LH in the energy band 0.5–2.0 keV. Our estimated minimum detectable flux allows us to determine the number of sources expected per square degree. We took into account the quadratic sum of two errors: an error of 10% on the flux, and an imprecision of 10% on the $\log(N) - \log(S)$ relation. Results are reported in Table 5.

As a consistency check, we processed a long observation of 90 ks of the LH that took place on November 27th 2002. This observation used a full frame window and a medium filter as for our observations. We performed exactly the same data processing that we used for our observations, and plotted the $\log(N) - \log(S)$ relation for the energy band 0.5–2 keV (see Fig. 4). We also plotted the $\log(N) - \log(S)$ relation using the sources detected in the same band with a correction for the higher absorption in the field of view of NGC 2808. The shape of the curves are similar, and we can see the flux detection limit in the different fields due to exposure time. The $\log(N) - \log(S)$ relation is therefore applicable to our data.

The results reported in Table 5 indicate that the five sources located in the center of the field of view are likely to be related to the cluster. The probability of membership if we assume a Poisson distribution is 99.9985%. Moreover a possible excess of sources appears in the annuli between radii $3.6'$ and $6.5'$ ($4.5 r_h$ to $8 r_h$). The probability of membership to the cluster is 96.75%. As we are dealing with low numbers, statistical fluctuations might explain this excess, but we have nonetheless included these sources in our analysis.

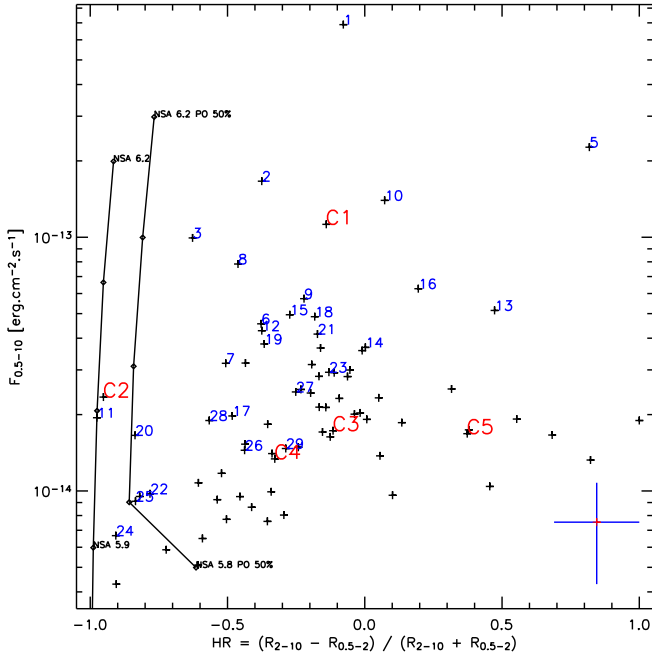
4.2. Spectral analysis

We first plotted the hardness ratios obtained during the source detection for sources with more than 50 counts and more than 3 counts in each energy band (Figs. 5 and 6). We show the tracks

¹ <http://heasarc.gsfc.nasa.gov/Tools/w3pimms.html>

Table 5. Expected and detected sources for NGC 2808 field of view.

Annulus ($^{\circ}$)	Expected 0.5–2 keV	Detected 0.5–2 keV
0 – 0.76	0.30 ± 0.06	5
0.76 – 3.6	6.27 ± 1.24	5
3.6 – 6.5	14.31 ± 2.94	20
6.5 – 9	17.58 ± 3.79	20
9 – 12	21.99 ± 5.88	20

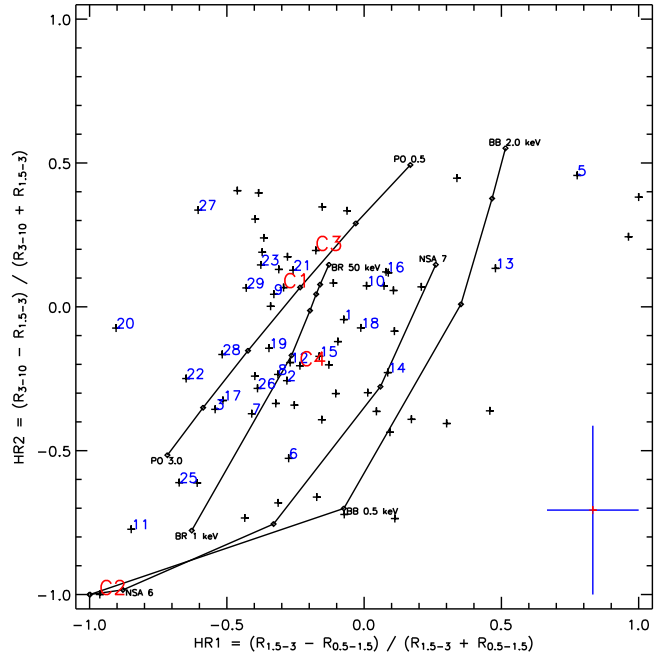
**Fig. 5.** Flux-colour diagram of NGC 2808 sources. For clarity, only the 30 brightest sources are enumerated, the flux values for all the sources are listed in Table 2. R is the count rate for the given energy band in keV. A typical error bar is shown at the bottom right. Black lines represent the following models, assuming an absorption of $1.2 \times 10^{21} \text{ cm}^{-2}$:

NSA: neutron star with hydrogen atmosphere, mass $1.4M_{\odot}$, radius 12 km, distance of the cluster and $\log(T_{\text{eff}}) = 5.9, 6, 6.1, 6.2$.

NSA PO: NSA and a power law with photon index of 1 and contributing 50% of the flux.

of some spectral models. In Fig. 5, possible qLMXBs are located on the left side of the diagram, while very absorbed sources are seen on the right side of the diagram. The most luminous and absorbed sources have colours that are similar to these of extragalactic objects as discussed in Sect. 6. In Fig. 6, the qLMXB candidates should be located at the bottom left, and CVs in the middle of the diagram around the power law branch with photon indices 1 to 1.5 and the bremsstrahlung branch with temperatures 10 to 50 keV (e.g. Richman 1996; Baskill et al. 2005).

For the brightest sources, we extracted and fitted the spectra. We used an extraction radius of $30''$ whenever possible, so 80% of the encircled energy was included. In the crowded region the extraction radius was reduced to $8''$, corresponding to 50% encircled energy (Ehle et al. 2006, §3.2.1). A correction is taken into account in the instrumental response files. We extracted a background with the same extraction radius for each

**Fig. 6.** Colour-colour diagram of NGC 2808 sources. Same comments as for Fig. 5.

PO: power law with photon indices 3, 2.5, 2, 1.5, 1, 0.5.

BR: thermal bremsstrahlung with temperatures 1, 5, 10, 15, 20, 50 keV.

BB: blackbody spectrum with temperatures 0.1, 0.5, 1, 1.5, 2 keV.

NSA: neutron star with hydrogen atmosphere, mass $1.4M_{\odot}$, radius 12 km, distance of the cluster and $\log(T_{\text{eff}}) = 5, 6, 6.5, 6.8, 7$.

source in a region without sources on the same CCD, with the same vignetting, and when possible at the same distance from CCD readout node for pn CCDs.

We used the task *evselect* with a binning of 15 eV for MOS data and 5 eV for pn data as recommended (Loiseau 2006, §4.9.1). Then for each spectrum we used *rmfgen* and *arfgen* to generate the instrumental response files for a point source, i.e. the redistribution matrix file (RMF) and the ancillary response file (ARF). We fitted the data with Xspec v11.3.2 (Arnaud 1996). A binning greater than 20 counts allowed the use of the χ^2 minimization criterion, but when there were insufficient counts per bin (under 20 per bin), we used the Cash statistic (Cash 1979) which provides a goodness-of-fit criterion similar to that of χ^2 .

We tried simple models included in Xspec such as a power law, a bremsstrahlung, a black body, a Raymond Smith or a mekal fit. For very soft sources we tried a hydrogen atmosphere model (Zavlin et al. 1996), assuming the distance of the GC, a mass of $1.4 M_{\odot}$ and a radius of 12 km for a neutron star. These parameters correspond to other neutron stars detected previously in GCs (Webb & Barret 2007; Heinke et al. 2003a). When it was clear that a simple model was insufficient to fit the data we tried composite models. The results of the spectral fitting are provided in Table 6 and are discussed in Sect. 6. We also provide the spectra of C1 and C2 (Figs. 7 and 8).

A global background spectrum was extracted for each EPIC camera in order to locate possible features in the background that could be present in the source spectra. We selected all regions without sources by excluding areas of $1'$ radius around

Table 6. Best fitting models to the spectra of sources in the NGC 2808 field of view. The unabsorbed flux is in the 0.5–10 keV range [$\times 10^{-14}$ erg cm $^{-2}$ s $^{-1}$] and for possible cluster sources the luminosity is given in the 0.5–10 keV range [$\times 10^{32}$ erg s $^{-1}$]. The models tried are a power law (PO), an absorbed power law (APL), a bremsstrahlung (BR), a black body (BB), a Raymond-Smith (RS), a mekal (MK) and a neutron star with hydrogen atmosphere (NSA). We used models with one or two components (Comp. 1 and Comp. 2). The absorption N_H gal [$\times 10^{21}$ cm $^{-2}$] is frozen to the value of the cluster. Parameter values are photon-index Γ of PO model, temperature kT [keV] of BB, RS and MK models, and $\log(T_{\text{eff}})$ [K] of NSA model. χ^2 and C give the goodness of the fit, reported with the number of degrees of freedom (*dof*).

Src ID	Flux (Lum)	$N_{H, \text{gal}}$	Model Comp. 1	N_H	Γ	kT	$\log(T_{\text{eff}})$	Model Comp. 2	Γ	kT	χ^2	C	<i>dof</i>
C1	8.6 ± 1.5 (9.5 ± 1.7)	1.2	PO	–	1.56 ± 0.14	–	–	–	–	–	–	37.54	43
			BR	–	–	–	$12.28^{+19.42}_{-5.03}$	–	–	–	–	–	37.35
C2	2.4 ± 0.3 (2.6 ± 0.4)	1.2	PO	–	2.8 ± 0.2	–	–	–	–	–	–	51.37	43
			NSA	0.98 ± 0.04	–	–	6.016 ± 0.017	–	–	–	–	56.45	43
			NSA	0.82 ± 0.40	–	–	5.975 ± 0.027	PO	1.56	–	–	–	38.88
1	52.8 ± 8.6	1.2	PO	–	1.31 ± 0.05	–	–	–	–	–	143.38	–	94
			APL	4.3 ± 1.8	1.7 ± 0.2	–	–	PO	4.7 ± 1.4	–	–	98.07	–
2	15.4 ± 1.2	1.2	PO	–	1.9 ± 0.1	–	–	–	–	–	48.28	–	36
3	9.1 ± 1.1	1.2	PO	–	2.6 ± 0.1	–	–	–	–	–	46.36	–	36
5	17.3 ± 2.7	1.2	APL	$35.03^{+18.63}_{-13.71}$	1.65 ± 0.60	–	–	–	–	–	27.17	–	20
			APL	$49.46^{+23.53}_{-10.57}$	$1.918^{+0.89}_{-0.53}$	–	–	PO	2.0	–	–	15.14	–
13	6.4 ± 0.7	1.2	PO	–	0.32 ± 0.25	–	–	–	–	–	–	53.95	38
			APL	$5.64^{+8.9}_{-4.93}$	$0.75^{+0.64}_{-0.42}$	–	–	PO	$9.5^{+0.5}_{-0.6}$	–	–	–	41.20
17	2.1 ± 0.6	1.2	PO	–	2.1 ± 0.3	–	–	–	–	–	–	28.95	27
			MK	–	–	2.7 ± 1.0	–	–	–	–	–	–	30.63
22	1.1 ± 0.6 (1.2 ± 0.6)	1.2	BB	–	–	0.16 ± 0.02	–	MK	–	76^{+14}_{-59}	–	49.54	40
24	0.9 ± 0.2 (1.0 ± 0.2)	1.2	RS	–	–	0.40 ± 0.09	–	–	–	–	–	29.62	27
25	0.9 ± 0.2 (1.0 ± 0.2)	1.2	BB	–	–	0.17 ± 0.09	–	MK	–	6.19 ± 6.1	–	18.71	25

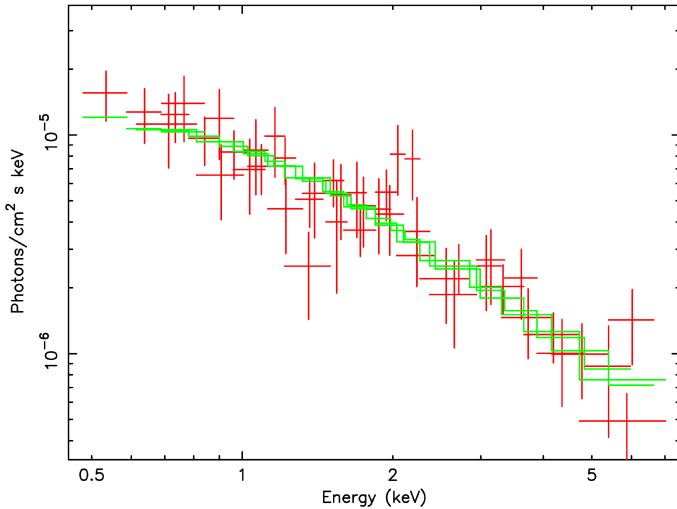


Fig. 7. Spectrum of C1 (NGC 2808) fitted with a power law model and the absorption of the cluster.

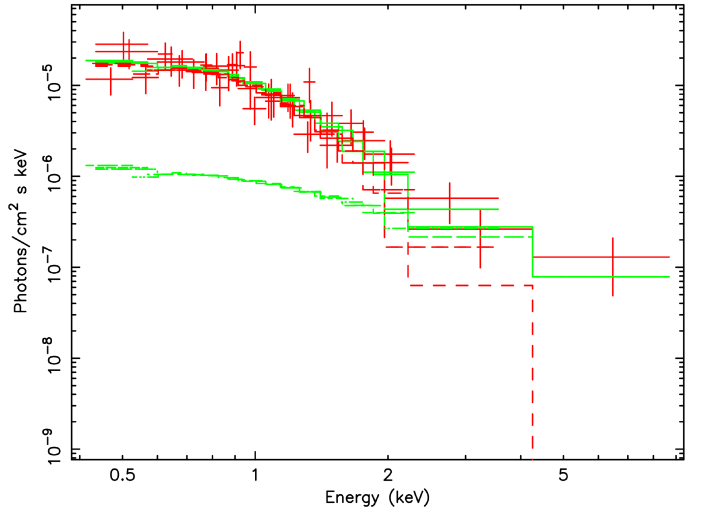


Fig. 8. Spectrum of C2 (NGC 2808) fitted with a NSA model and the absorption of the cluster. The contribution of C1 also appears as a power law.

detected sources. We produced the instrumental response files for a flat field. Based on this spectrum, we fixed the limits of the energy bands we used: 0.4–15 keV for pn events, and 0.2–10 keV for MOS events. For all sources we could evaluate the flux in the 0.5–10 keV energy band. For MOS, two strong lines are observed at 1.5 and 1.75 keV (Al $K\alpha$ and Si $K\alpha$ lines). For pn, the background spectrum shows a strong line feature around 1.5 keV (Al $K\alpha$ line), fainter lines at 8 and 8.6 keV (Cu lines), and some features at 9.7 and 11 keV (as seen in Ehle et al. 2006, §3.3.7).

4.3. Variability analysis

We performed variability analysis based on the pn data for sources with more than 300 pn counts, and for sources with a fitted spectrum and more than 100 pn counts. We extracted lightcurves for sources and backgrounds (same regions as for spectral analysis), adjusting the binning for each source to obtain a mean of 20 counts per bin after correction. We removed the first 12 ks of the observation as this part is affected by flares. We corrected the pn events for losses due to e.g. vignetting or

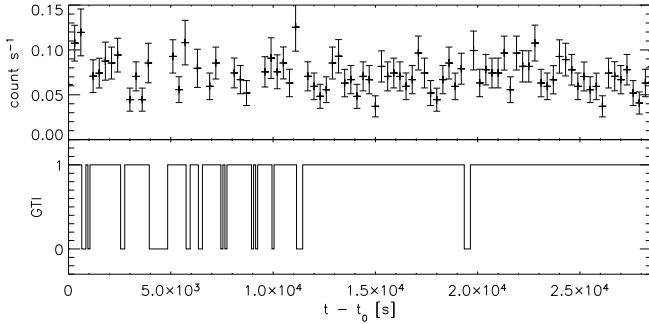


Fig. 9. Lightcurve of source 1 (NGC 2808) and corresponding good time intervals (GTI) as defined in Sect. 2.1. Start time t_0 is February 1st 2005 4:57:28 (MJD 2453402.70657).

Table 7. Variability analysis of NGC 2808 sources. We give for each source the Bin size [s], the Kolmogorov-Smirnov probability of the source lightcurve being differently distributed than the background lightcurve (K-S), and the χ^2 with the number of degrees of freedom (*dof*) for the background subtracted lightcurve fitted with a constant.

ID	Bin size	K-S	χ^2	<i>dof</i>
C1	2400	0.15	6.08	10
C2	3000	0.31	20.05	9
1	300	1.05×10^{-4}	120.90	82
2	600	0.23	48.71	39
3	600	0.04	67.87	39
5	1200	0.33	31.90	21
13	2000	0.86	23.65	13
17	2400	0.15	31.08	10

filters with the SAS task *lccorr*. The time variability is examined with a Kolmogorov-Smirnov test using IDL/Astrolib² procedure *kstwo* by comparing the source lightcurve to the background lightcurve. We also fitted the background subtracted lightcurve with a constant value, and calculated the χ^2 of the fit. The results are reported in Table 7. Only source 1 seems to be variable with a significant probability. The lightcurve is presented in Fig. 9 and discussed in Sect. 6.6.

5. The X-ray sources in NGC 4372

Johnston et al. (1996) found 9 sources in NGC 4372 with the ROSAT X-ray observatory in an equivalent region of the sky covered by our XMM-Newton observation. Two of these sources were not detected in our observations (R8 and R10), and we detect three additional sources (7, 8 and 9). Three merged sources in the ROSAT image (R5, R7 and R8) are clearly resolved into two bright sources (1 and 2) and one faint and more diffuse source (9), see Fig. 3.

We could not use a $\log(N) - \log(S)$ relation to discuss the distribution of sources, as in Sect. 4.1 for NGC 2808, because of the low number of sources detected which leads to large error bars. Moreover the high background noise due to high flaring activity does not allow us to estimate accurately the flux detection limit. From the faintest sources detected, this limit is around $F_{0.5-10 \text{ keV}} \sim 3 \pm 1 \times 10^{-14} \text{ erg cm}^{-2} \text{ s}^{-1}$, which leads to a limiting luminosity of $L_{0.5-10 \text{ keV}} \sim 10^{32} \text{ erg s}^{-1}$ for a source in the core of the cluster. From the count rate of the faintest sources detected by ROSAT in this region, their limiting flux (obtained with

² <http://idlastro.gsfc.nasa.gov/>

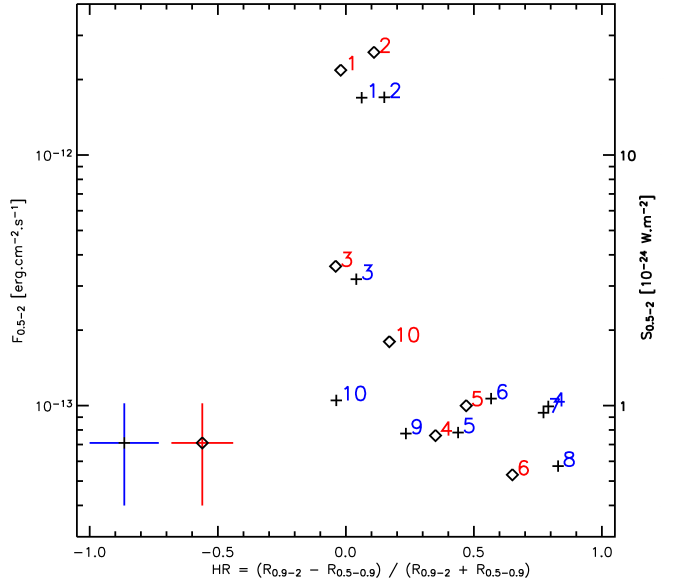


Fig. 10. Flux-colour diagram of NGC 4372 sources detected with XMM-Newton (crosses, units on the left axis) and ROSAT (diamonds, units on the right axis). R is the count rate for the given energy band in keV. Typical error bars are shown at the bottom left.

Table 8. Best fitting models to spectra of sources in the NGC 4372 field of view. Same as Table 6.

Src	Flux	$N_{H, gal}$	Model	Γ	kT	χ^2	<i>dof</i>
1	148 ± 10	2.8	PO	4.1 ± 0.2	–	155.94	113
			BB	–	0.14 ± 0.01	153.70	113
2	147 ± 10	2.8	PO	4.1 ± 0.2	–	100.40	79
			BB	–	0.14 ± 0.01	99.02	79

WebPIMMS) is $F_{0.5-10 \text{ keV}} \sim 5 \pm 2 \times 10^{-14} \text{ erg cm}^{-2} \text{ s}^{-1}$, so we expect to detect all ROSAT sources in this region. We note that our flux detection limit is comparable to the ROSAT limit, due to large cuts after flare filtering and the absence of pn data, but we increase the angular resolution and clearly resolve the sources.

We performed the same analysis as in Sect. 4.2. We carried out spectral analysis for two sources with sufficient counts, in the same manner as described in Sect. 4.2. The results are reported in Table 8.

We compared hardness ratios given by Johnston et al. (1996) to the ones we obtained using the same energy bands. We plotted for both ROSAT and XMM-Newton data a flux-colour diagram (Fig. 10). The two distributions are well correlated within the error bars, especially for bright sources, but we note that source 4 seems harder in our observation.

6. Discussion

We discuss here the presence of objects expected in globular clusters such as qLMXBs, CVs, MSPs and ABs, adding notes on individual sources. We also discuss some background and foreground sources which present unusual features.

6.1. Low mass X-ray binaries in quiescence

For 18 GCs that have been observed deep enough to detect all qLMXBs, we plotted the number of qLMXBs against the

approximate encounter rate for a virialized system ($\rho_0^{1.5} r_c^2$), as done in Gendre et al. (2003a). According to this correlation, one would expect 3 ± 1 qLMXBs in NGC 2808, and none in NGC 4372.

For NGC 2808 we detect one source consistent with a qLMXB (C2, described below). For NGC 4372, a qLMXB having the minimum luminosity of the 21 qLMXBs reported by Heinke et al. (2003b) would have been detected. The lack of detection is therefore consistent with the prediction of zero qLMXB in this cluster.

NGC 2808 – C2. This source is located in the core radius of NGC 2808. It is close to a bright source (C1, $15''$) and the PSF wings are merged. From Ehle et al. (2006, §3.2.1), we estimated that 10% of the emission of C1 was present in the C2 spectrum. We fitted a model composed of 10% of the C1 spectrum and a hydrogen atmosphere model for a neutron star. The parameters are given in Table 6 and the spectrum in Fig. 8. The hard emission in this spectrum appears to be due to C1. We note that the unabsorbed luminosity ($2.6 \pm 0.4 \times 10^{32}$ erg s $^{-1}$ if it belongs to the cluster), and the X-ray spectrum of C2 are consistent with the qLMXB hypothesis.

6.2. Cataclysmic variables

Ivanova et al. (2006), using numerical simulations and taking into account different CV formation channels, predict about 200 CVs for a GC similar to NGC 2808. Of these, only a fraction can be detected in our data. From the empirical function of Pooley & Hut (2006) derived from fitting the number of bright CVs (at luminosities above $L_{0.5-10 \text{ keV}} = 4.25 \times 10^{31}$ erg s $^{-1}$) against the specific encounter frequency, we estimate a population of 20^{+20}_{-10} bright CVs in NGC 2808. Given the X-ray unabsorbed luminosity of the core (excluding C2) of $L_{0.5-10 \text{ keV}} = 1.4 \times 10^{33}$ erg s $^{-1}$, we cannot expect more than 30 bright CVs in this region.

We detect 4 CV candidates in NGC 2808 with luminosities down to $L_{0.5-10 \text{ keV}} \sim 3.0 \times 10^{32}$ erg s $^{-1}$. A hidden unresolved population of fainter CVs may exist in the core of the cluster, but only the brightest have been detected in our observation. In particular, we note that the source C1 has a luminosity ($L_{0.5-10 \text{ keV}} = 9.5 \times 10^{32}$ erg s $^{-1}$ if it belongs to the cluster) higher than the known luminosities of CVs (Verbunt et al. 1994), and could be composed of several sources. After removing the contribution of C2 from the core global spectrum we found a spectral photon-index of $\Gamma = 1.44 \pm 0.09$, consistent with CV emission (e.g. Baskill et al. 2005), and only the brightest MSPs emission (Bogdanov et al. 2005). This supports the idea that the core emission is due to a majority of CVs.

In NGC 4372 which is a less massive cluster, the estimation leads to less than one bright CV. If CVs are present in the cluster, they must be fainter than our limiting luminosity.

NGC 2808 – C1. Source C1 is located in the core radius of NGC 2808. This source is hard, and is well fitted with a power law model or a bremsstrahlung model (see Table 6). These values are consistent with CV X-ray emission (e.g. Richman 1996; Baskill et al. 2005). C1 also has a UV counterpart (UV 222) proposed to be a CV by Dieball et al. (2005), strengthening this hypothesis. The spectrum is plotted in Fig. 7. At 2.0 keV, a feature that at first sight could be an emission line is not well fitted with a Gaussian. It is possibly due

to the fact that CV1 emission may be complex emission from several sources, as its luminosity is quite high for a single CV.

NGC 2808 – C3, C4, C5. These sources are located in the half-mass radius and the colours indicate that they are likely to be CVs (Fig. 6 and 5, and Table 2). Their luminosity, if they are members of the cluster is consistent with this hypothesis.

6.3. Millisecond pulsars in NGC 2808?

Some GCs are known to harbour a large population of MSPs. In 47 Tuc, which is similar in mass to NGC 2808, a population of ~ 25 MSPs is estimated (Heinke et al. 2005). The brightest MSPs have luminosities around our flux detection limit for NGC 2808. However, we note that MSPs, which are hard X-ray sources, are difficult to distinguish from CVs at this luminosity (Bogdanov et al. 2005). Therefore, our observations are not constraining for the presence of MSPs in NGC 2808. For NGC 4372, their flux is too faint to be detected.

6.4. Other sources possibly linked to NGC 2808

We detect 5 sources with a hardness ratio below -0.7 in the flux-colour diagram presented in Fig. 5, and located $\sim 5 - 6 \times r_{h[NGC2808]}$ away. Such sources could explain the possible excess of sources found in Sect. 4.1 if some are linked to the cluster. There is a high probability that these sources are background sources, but if they are linked to the cluster, they could have been formed from primordial binaries and remain outside of the half-mass radius (Hurley et al. 2007).

Dempsey et al. (1993) presented a study of 44 RS CVn systems (ABs) observed with the ROSAT observatory, and showed that their spectra are very soft with most of the emission below 2 keV. From their spectra (Table 6), colours and luminosity, sources 24 and 41 have similarities with the brightest ABs.

Evans & Hellier (2007) used a black body model to fit the soft excess below 2 keV found in the spectra of some intermediate polars, the hard emission of intermediate polars being fitted with a mekal model. Sources 22, 25 and 50 have soft spectra with a hard tail (Table 6), and could therefore be intermediate polars.

Some of the soft sources could also be active stars in the foreground. The X-ray flux here is consistent with an estimated distance of ~ 100 pc.

6.5. Looking for an IMBH in NGC 2808

Following Trenti (2006), NGC 2808 is a good candidate for hosting an IMBH as the ratio r_c/r_h is larger than the critical threshold of 0.3. This cluster may however not be sufficiently relaxed as the age is only 7.4 times the half-mass relaxation time (Hurley 2007).

If such an IMBH exists in NGC 2808, it should be located at the center of mass of the cluster due to mass segregation. We found no evidence for an X-ray source at this position but it may be below our detection limit. We assume that the BH is fed by intracluster gas with a density of ~ 0.5 cm $^{-3}$ derived from Pfahl & Rappaport (2001) with NGC 2808 parameters. It should be noted, however, that a possible detection of 200 M_\odot of neutral hydrogen in the core of NGC 2808 has been reported in the literature (Faulkner et al. 1991). If this is confirmed, it implies that the gas density is underestimated here. In the same way as Ho et al. (2003), if we assume a BH of 1 000 M_\odot accreting at

the full Bondi rate (Bondi 1952) and an optically thick, geometrically thin disk (Shakura & Syunyaev 1973), we found an X-ray accretion luminosity five orders of magnitude above our limiting luminosity. However, the BH may be radiatively inefficient as for optically thin advection-dominated accretion flow (ADAFs, see e.g. Narayan et al. 1998). Following Grindlay et al. (2001), our limiting luminosity implies an upper limit of $\sim 290 M_{\odot}$ for a central IMBH in NGC 2808.

6.6. Other NGC 2808 sources

NGC 2808 – 1. This source is the brightest source in the field of view, located 8.5' away from the center of NGC 2808. A source was previously listed in the ASCA source catalogue (Ueda et al. 2001) with a compatible position. The unabsorbed flux is lower but consistent with our detection ($F_{0.7-7 \text{ keV}}^{\text{ASCA}} = 3.0 \pm 0.7 \times 10^{-13} \text{ erg cm}^{-2} \text{ s}^{-1}$ and $F_{0.7-7 \text{ keV}}^{\text{XMM}} = 4.0 \pm 0.5 \times 10^{-13} \text{ erg cm}^{-2} \text{ s}^{-1}$).

This source is well fitted with the absorbed power law model (APL+PO) used by Mainieri et al. (2007) for Seyfert 2 active galactic nuclei (AGN) spectra. It is composed of the Galactic absorption, an absorbed power law, and an unabsorbed power law to model the soft excess below 0.9 keV. The lightcurve plotted in Fig. 9 is typical of an AGN, showing short-term low amplitude variability (see for instance Gliozzi et al. 2004). We note that a UV counterpart is found in the OM data. These features are all consistent with an AGN, but an optical or infrared counterpart is needed to confirm the nature of this source.

NGC 2808 – 5 and 13. These sources show very absorbed spectra, well fitted with the APL+PO model (Mainieri et al. 2007). These spectra could indicate Seyfert 2 AGN, as for source 1.

NGC 2808 – 17. This source is located 3.2' away from the center of NGC 2808. We found a possible optical counterpart, HD 79548 at RA₂₀₀₀ 9^h11^m33.293^s, Dec₂₀₀₀ -64°51'03.28". This star is an A0V star with magnitudes $B = 10.42$ and $V = 10.15$. A UV counterpart is observed in the OM data with a magnitude of 10.95, consistent with the emission of HD 79548. Using the distance and the visual magnitude of Vega, a well known A0V star (7.76 pc, $V = 0.03$), we estimated a distance of ~ 800 pc for HD 79548, and derived an X-ray luminosity of $L_{0.5-10 \text{ keV}} = 4.9 \pm 0.9 \times 10^{29} \text{ erg s}^{-1}$.

The relation between the X-ray source and HD 79548 is unclear and it is possible that we observe a background source aligned with HD 79548. However, young A0V stars with an age less than 10^7 yr can be such a bright X-ray source (e.g. Pease et al. 2006; Tout & Pringle 1995). An active star as a companion is also consistent with the X-ray emission obtained (Briggs & Pye 2003; Golub et al. 1983). Optical spectroscopic observations of this source could help to determine the nature of this object.

6.7. Peculiar NGC 4372 sources

As the sources are distant from the core of the GC, they are more likely to be background sources.

NGC 4372 – 1 and 2. These two soft sources appear to have similar parameters (Table 8). They are around 12' away from the center of NGC 4372, and are 2' away from each other. Their

spectra show a soft excess between 0.5 and 0.9 keV, possibly due to reprocessed emission of an absorbed AGN.

NGC 4372 – 4. This source appears to be harder than the source R13 detected previously with ROSAT at the same location (within the error circles). With ROSAT, the photon-index corresponding to the hardness ratio is ~ 2 , and for our observation, it goes down to ~ 0.5 , if we assume the same absorption. If we assume the same photon-index for the two observations, then the absorption has doubled.

NGC 4372 – 7, 8 and R10. In the contour map published by Johnston et al. (1996), we can see some unresolved features at the positions of sources 7 and 8. We can estimate that their fluxes (Table 3) have increased by a factor 12 and 4 for sources 7 and 8 respectively. ROSAT source R10 is not detected in our data. As we should have detected all ROSAT sources, it may have varied between the two observations by a factor 2 to become fainter than our limiting flux.

7. Conclusions

We have presented XMM-Newton observations of the globular clusters NGC 2808 and NGC 4372.

For NGC 2808, we have shown that the five central sources are likely to be linked to the cluster. One of these is very likely to be a qLMXB, and the emission of the remaining central sources is consistent with 20 ± 10 bright CVs (at luminosities above $L_{0.5-10 \text{ keV}} = 4.25 \times 10^{31} \text{ erg s}^{-1}$), of which 4 are detected in our data. A summary of these sources is presented in Table 9. We expect to resolve more objects in the core of NGC 2808 in our Chandra observation (Servillat et al. 2008).

For NGC 4372, we detect no sources in the half-mass radius, but the limiting luminosity of our observations is not constraining, in particular for a possible population of faint CVs. We compared our sources outside the half-mass radius to previously detected sources with ROSAT in the field of view, and found a very good correlation for most of the sources.

Acknowledgements. This work is based on observations obtained with XMM-Newton, an ESA science mission with instruments and contributions directly funded by ESA Member States and NASA. We thank the CNES for support of the operational phase of the mission. This research has made use of the SIMBAD database, operated at the CDS, Strasbourg, France. We are grateful to J. Grindlay whose comments have helped to improve this paper.

References

- Alcaino, G., Liller, W., Alvarado, F., & Wenderoth, E. 1991, *AJ*, 102, 159
- Arnaud, K. A. 1996, in *ASP Conf. Ser. 101: Astronomical Data Analysis Software and Systems V*, ed. G. H. Jacoby & J. Barnes, 17
- Baskill, D. S., Wheatley, P. J., & Osborne, J. P. 2005, *MNRAS*, 357, 626
- Bedin, L. R., Piotto, G., Zoccali, M., et al. 2000, *A&A*, 363, 159
- Bogdanov, S., Grindlay, J. E., & van den Berg, M. 2005, *ApJ*, 630, 1029
- Bondi, H. 1952, *MNRAS*, 112, 195
- Briggs, K. R. & Pye, J. P. 2003, *MNRAS*, 345, 714
- Burstein, D. & Heiles, C. 1978, *Astrophys. Lett.*, 19, 69
- Carretta, E., Bragaglia, A., Gratton, R. G., et al. 2006, *A&A*, 450, 523
- Carretta, E., Gratton, R. G., Clementini, G., & Fusi Pecci, F. 2000, *ApJ*, 533, 215
- Cash, W. 1979, *ApJ*, 228, 939
- Colpi, M., Mapelli, M., & Possenti, A. 2003, *ApJ*, 599, 1260
- D'Amico, N., Possenti, A., Fici, L., et al. 2002, *ApJ*, 570, L89
- Dempsey, R. C., Linsky, J. L., Schmitt, J. H. M. M., & Fleming, T. A. 1993, *ApJ*, 413, 333
- Dieball, A., Knigge, C., Zurek, D. R., Shara, M. M., & Long, K. S. 2005, *ApJ*, 625, 156

Table 9. NGC 2808 core sources summary table. We give for each source the J2000 position with errors, the offset from the GC center, the luminosity in band 0.5–10 keV [$\times 10^{-14}$ erg s $^{-1}$] and the hardness ratios (*HR*). The probable nature of the object is indicated as discussed in Sect. 6. The *HR* for two energy band *B1* and *B2* are defined by $HR = (B2 - B1)/(B1 + B2)$, *HR1* for 0.5–1.5 and 1.5–3 keV energy bands, *HR2* for 1.5–3 and 3–10 keV energy bands.

ID	RA ₂₀₀₀	Dec ₂₀₀₀	Error	Offset	Lum.	HR1	HR2	Probable nature
C1	9 ^h 12 ^m 04.33 ^s	-64°51′49.09″	3.47″	0.19′	9.5±1.7	-0.29	0.07	CV
C2	9 ^h 12 ^m 01.65 ^s	-64°51′51.58″	3.07″	0.13′	2.6±0.4	-0.96	-1.00	qLMXB
C3	9 ^h 12 ^m 00.58 ^s	-64°52′00.14″	3.43″	0.31′	3.3±2.0	-0.18	0.20	CV
C4	9 ^h 12 ^m 03.85 ^s	-64°52′04.50″	4.47″	0.32′	3.2±2.1	-0.23	-0.20	CV
C5	9 ^h 11 ^m 59.27 ^s	-64°51′46.74″	4.47″	0.35′	3.0±1.8	0.33	0.08	CV

- Edmonds, P. D., Gilliland, R. L., Heinke, C. O., & Grindlay, J. E. 2003, *ApJ*, 596, 1177
- Ehle, M., Breitfellner, M., Gonzalez Riestra, R., et al. 2006, XMM-Newton Users' Handbook v2.4
- Evans, P. A. & Hellier, C. 2007, *ApJ*, 663, 1277
- Faulkner, D. J., Scott, T. R., Wood, P. R., & Wright, A. E. 1991, *ApJ*, 374, L45
- Gebhardt, K., Rich, R. M., & Ho, L. C. 2002, *ApJ*, 578, L41
- Gebhardt, K., Rich, R. M., & Ho, L. C. 2005, *ApJ*, 634, 1093
- Gendre, B., Barret, D., & Webb, N. A. 2003a, *A&A*, 403, L11
- Gendre, B., Barret, D., & Webb, N. A. 2003b, *A&A*, 400, 521
- Gerssen, J., van der Marel, R. P., Gebhardt, K., et al. 2002, *AJ*, 124, 3270
- Gliozzi, M., Sambruna, R. M., Brandt, W. N., Mushotzky, R., & Eracleous, M. 2004, *A&A*, 413, 139
- Golub, L., Harnden, Jr., F. R., Maxson, C. W., et al. 1983, *ApJ*, 271, 264
- Grindlay, J. E., Heinke, C., Edmonds, P. D., & Murray, S. S. 2001, *Science*, 292, 2290
- Harris, W. E. 1974, *ApJ*, 192, L161
- Harris, W. E. 1996, *AJ*, 112, 1487
- Hasinger, G., Miyaji, T., & Schmidt, M. 2005, *A&A*, 441, 417
- Heinke, C. O., Grindlay, J. E., Edmonds, P. D., et al. 2005, *ApJ*, 625, 796
- Heinke, C. O., Grindlay, J. E., Lloyd, D. A., & Edmonds, P. D. 2003a, *ApJ*, 588, 452
- Heinke, C. O., Grindlay, J. E., Lugger, P. M., et al. 2003b, *ApJ*, 598, 501
- Heinke, C. O., Wijnands, R., Cohn, H. N., et al. 2006, *ApJ*, 651, 1098
- Ho, L. C., Terashima, Y., & Okajima, T. 2003, *ApJ*, 587, L35
- Hurley, J. R. 2007, *MNRAS*, 379, 93
- Hurley, J. R., Aarseth, S. J., & Shara, M. M. 2007, *ApJ*, 665, 707
- Hut, P., McMillan, S., Goodman, J., et al. 1992, *PASP*, 104, 981
- Hut, P., Shara, M. M., Aarseth, S. J., et al. 2003, *New Astronomy*, 8, 337
- Ivanova, N., Heinke, C. O., Rasio, F. A., et al. 2006, *MNRAS*, 372, 1043
- Johnston, H. M., Verbunt, F., & Hasinger, G. 1996, *A&A*, 309, 116
- Kaluzny, J. & Krzeminski, W. 1993, *MNRAS*, 264, 785
- Lewin, W. H. G. & Joss, P. C. 1983, in *Accretion-Driven Stellar X-ray Sources*, ed. W. H. G. Lewin & E. P. J. van den Heuvel, 41
- Lightman, A. P. & Grindlay, J. E. 1982, *ApJ*, 262, 145
- Lockman, F. J., Jahoda, K., & McCammon, D. 1986, *ApJ*, 302, 432
- Loiseau, N. 2006, User's Guide to the XMM-Newton Science Analysis System v4.0
- Maccarone, T. J., Kundu, A., Zepf, S. E., & Rhode, K. L. 2007, *Nature*, 445, 183
- Maineri, V., Hasinger, G., Cappelluti, N., et al. 2007, *ApJS*, 172, 368
- Mukai, K. 1993, *Legacy*, vol. 3, p.21-31, 3, 21
- Narayan, R., Mahadevan, R., & Quataert, E. 1998, in *Theory of Black Hole Accretion Disks*, ed. M. A. Abramowicz, G. Bjornsson, & J. E. Pringle, 148
- Pease, D. O., Drake, J. J., & Kashyap, V. L. 2006, *ApJ*, 636, 426
- Pfahl, E. & Rappaport, S. 2001, *ApJ*, 550, 172
- Pietrukowicz, P., Kaluzny, J., Thompson, I. B., et al. 2005, *Acta Astronomica*, 55, 261
- Piotto, G., Bedin, L. R., Anderson, J., et al. 2007, *ApJ*, 661, L53
- Pooley, D. & Hut, P. 2006, *ApJ*, 646, L143
- Pooley, D., Lewin, W. H. G., Anderson, S. F., et al. 2003, *ApJ*, 591, L131
- Richman, H. R. 1996, *ApJ*, 462, 404
- Servillat, M., Webb, N. A., Barret, D., et al. 2008, in *IAU Symposium 246, Dynamical Evolution of Dense Stellar Systems*, ed. E. Vesperini, M. Giersz, & A. Sills, submitted
- Shakura, N. I. & Syunyaev, R. A. 1973, *A&A*, 24, 337
- Tout, C. A. & Pringle, J. E. 1995, *MNRAS*, 272, 528
- Trenti, M. 2006, *MNRAS*, submitted (astro-ph/0612040)
- Trenti, M., Ardi, E., Mineshige, S., & Hut, P. 2007, *MNRAS*, 374, 857
- Ueda, Y., Ishisaki, Y., Takahashi, T., Makishima, K., & Ohashi, T. 2001, *ApJS*, 133, 1
- Verbunt, F. & Hut, P. 1987, in *IAU Symp. 125: The Origin and Evolution of Neutron Stars*, ed. D. J. Helfand & J.-H. Huang, 187
- Verbunt, F., Johnston, H., Hasinger, G., Belloni, T., & Bunk, W. 1994, in *Astronomical Society of the Pacific Conference Series*, Vol. 56, *Interacting Binary Stars*, ed. A. W. Shafter, 244
- Voges, W., Aschenbach, B., Boller, T., et al. 1999, *A&A*, 349, 389
- Webb, N. A. & Barret, D. 2007, *ApJ*
- Webb, N. A., Serre, D., Gendre, B., et al. 2004, *A&A*, 424, 133
- Webb, N. A., Wheatley, P. J., & Barret, D. 2006, *A&A*, 445, 155
- Yang, Y., Mushotzky, R. F., Barger, A. J., et al. 2003, *ApJ*, 585, L85
- Zavlin, V. E., Pavlov, G. G., & Shibunov, Y. A. 1996, *A&A*, 315, 141

Online Material

Table 2. NGC 2808 X-ray source properties. The columns contain the ID of the source, the position (RA₂₀₀₀ and Dec₂₀₀₀) with the error, the rate [$\times 10^{-3}$ count s⁻¹], the flux converted with ECFs in band 0.5–10 keV [$\times 10^{-14}$ erg cm⁻² s⁻¹] and the hardness ratios (*HR*). The *HR* for two energy band *B1* and *B2* are defined by $HR = (B2 - B1)/(B1 + B2)$, *HR1* for 0.5–1.5 and 1.5–3 keV energy bands, *HR2* for 1.5–3 and 3–10 keV energy bands.

ID	RA ₂₀₀₀	Dec ₂₀₀₀	Error	Rate	Flux	<i>HR1</i>	<i>HR2</i>
C1	9 ^h 12 ^m 04.33 ^s	-64°51'49.09"	3.47"	29.1 ± 5.8	9.1 ± 4.2	-0.29	0.07
C2	9 ^h 12 ^m 01.65 ^s	-64°51'51.58"	3.07"	18.5 ± 4.4	2.5 ± 1.5	-0.96	-1.00
C3	9 ^h 12 ^m 00.58 ^s	-64°52'00.14"	3.43"	10.4 ± 2.4	3.0 ± 1.8	-0.18	0.20
C4	9 ^h 12 ^m 03.85 ^s	-64°52'04.50"	4.47"	7.9 ± 2.3	2.9 ± 1.9	-0.23	-0.20
C5	9 ^h 11 ^m 59.27 ^s	-64°51'46.74"	4.47"	5.9 ± 1.8	2.7 ± 1.6	0.33	0.08
1	9 ^h 10 ^m 49.68 ^s	-64°48'15.73"	2.73"	223.9 ± 5.1	71.4 ± 4.2	-0.07	-0.04
2	9 ^h 11 ^m 28.05 ^s	-64°50'37.34"	2.73"	72.8 ± 2.3	17.0 ± 1.5	-0.28	-0.26
3	9 ^h 11 ^m 18.94 ^s	-64°51'00.39"	2.73"	58.2 ± 2.1	9.7 ± 1.0	-0.54	-0.36
5	9 ^h 12 ^m 56.89 ^s	-64°52'28.86"	2.75"	48.7 ± 2.9	30.1 ± 4.3	0.78	0.46
6	9 ^h 13 ^m 01.41 ^s	-64°52'17.62"	2.78"	17.9 ± 1.2	3.7 ± 0.8	-0.27	-0.53
7	9 ^h 12 ^m 18.36 ^s	-64°48'41.90"	2.77"	15.7 ± 1.1	3.1 ± 0.6	-0.41	-0.37
8	9 ^h 13 ^m 41.37 ^s	-64°44'30.49"	2.79"	38.7 ± 2.9	9.4 ± 2.2	-0.31	-0.24
9	9 ^h 12 ^m 49.16 ^s	-64°44'49.84"	2.80"	20.9 ± 1.6	6.1 ± 1.3	-0.33	0.04
10	9 ^h 13 ^m 27.75 ^s	-64°43'20.61"	2.79"	39.3 ± 2.9	14.5 ± 2.7	0.01	0.07
11	9 ^h 12 ^m 25.55 ^s	-65°01'03.40"	2.81"	20.9 ± 1.7	2.0 ± 0.5	-0.85	-0.77
12	9 ^h 11 ^m 37.75 ^s	-64°44'04.26"	2.80"	18.5 ± 1.6	4.6 ± 1.2	-0.27	-0.19
13	9 ^h 11 ^m 26.44 ^s	-64°53'15.84"	2.80"	10.7 ± 0.9	5.4 ± 1.0	0.48	0.13
14	9 ^h 12 ^m 49.98 ^s	-64°56'13.02"	2.79"	11.2 ± 1.0	3.4 ± 0.8	0.09	-0.23
15	9 ^h 12 ^m 51.95 ^s	-65°02'12.43"	2.81"	19.3 ± 1.8	5.3 ± 1.4	-0.16	-0.17
16	9 ^h 13 ^m 37.17 ^s	-64°52'01.33"	2.83"	17.0 ± 1.6	6.6 ± 1.5	0.08	0.12
17	9 ^h 11 ^m 33.49 ^s	-64°51'04.13"	2.82"	8.4 ± 0.8	1.6 ± 0.5	-0.51	-0.33
18	9 ^h 13 ^m 01.98 ^s	-64°44'56.08"	2.90"	13.6 ± 1.6	4.9 ± 1.4	-0.01	-0.07
19	9 ^h 10 ^m 57.78 ^s	-64°49'36.80"	2.85"	16.4 ± 1.9	4.0 ± 1.1	-0.35	-0.14
20	9 ^h 13 ^m 28.80 ^s	-64°59'18.90"	2.85"	12.4 ± 1.5	1.9 ± 0.9	-0.90	-0.07
21	9 ^h 12 ^m 42.59 ^s	-65°01'25.98"	2.83"	16.3 ± 1.6	5.3 ± 1.4	-0.26	0.13
22	9 ^h 12 ^m 35.07 ^s	-64°53'17.99"	2.86"	6.8 ± 0.7	1.2 ± 0.4	-0.65	-0.25
23	9 ^h 12 ^m 36.92 ^s	-64°45'45.28"	2.90"	9.8 ± 1.1	3.1 ± 0.9	-0.38	0.15
24	9 ^h 12 ^m 01.49 ^s	-64°56'14.25"	2.85"	5.8 ± 0.7	0.9 ± 0.4	-0.99	-0.38
25	9 ^h 11 ^m 28.92 ^s	-64°55'23.47"	2.85"	6.4 ± 0.8	0.9 ± 0.4	-0.67	-0.61
26	9 ^h 12 ^m 26.97 ^s	-64°48'49.42"	2.88"	6.6 ± 0.8	1.3 ± 0.5	-0.39	-0.28
27	9 ^h 13 ^m 23.49 ^s	-64°51'04.73"	2.87"	9.8 ± 1.2	2.8 ± 1.0	-0.60	0.34
28	9 ^h 11 ^m 57.53 ^s	-65°02'53.79"	2.94"	9.7 ± 1.3	1.8 ± 0.9	-0.52	-0.17
29	9 ^h 12 ^m 02.18 ^s	-64°55'08.08"	2.87"	5.8 ± 0.7	1.6 ± 0.5	-0.43	0.07
30	9 ^h 11 ^m 06.52 ^s	-65°01'56.63"	2.89"	10.0 ± 1.4	3.0 ± 1.2	0.17	-0.39
31	9 ^h 13 ^m 12.59 ^s	-64°52'57.75"	2.91"	5.9 ± 0.8	1.1 ± 0.6	-0.31	-0.68
32	9 ^h 09 ^m 55.01 ^s	-64°51'10.46"	3.03"	15.8 ± 2.5	3.9 ± 2.0	-0.40	-0.24
33	9 ^h 10 ^m 42.43 ^s	-64°58'00.14"	2.98"	10.4 ± 1.6	2.9 ± 1.2	-0.10	-0.30
34	9 ^h 11 ^m 37.72 ^s	-64°46'02.15"	2.99"	6.8 ± 0.9	1.6 ± 0.7	-0.15	-0.39
35	9 ^h 10 ^m 26.42 ^s	-64°55'29.70"	2.94"	10.1 ± 1.4	4.0 ± 1.5	-0.31	0.13
36	9 ^h 12 ^m 42.88 ^s	-64°44'34.46"	3.03"	7.3 ± 1.1	2.3 ± 1.0	-0.11	0.08
37	9 ^h 12 ^m 33.26 ^s	-64°50'28.09"	2.93"	4.9 ± 0.7	2.2 ± 0.7	0.11	0.06
38	9 ^h 11 ^m 17.38 ^s	-64°46'54.15"	2.90"	9.0 ± 1.4	2.3 ± 1.0	-0.34	0.00
39	9 ^h 10 ^m 27.64 ^s	-65°00'59.56"	3.03"	11.6 ± 1.9	3.6 ± 1.9	-0.13	-0.20
40	9 ^h 12 ^m 54.61 ^s	-64°41'00.71"	3.17"	12.7 ± 2.0	3.6 ± 1.7	0.07	0.07
41	9 ^h 12 ^m 34.56 ^s	-64°53'47.62"	2.98"	3.3 ± 0.5	0.4 ± 0.2	-0.95	-0.34
42	9 ^h 13 ^m 49.91 ^s	-64°44'30.75"	3.20"	9.2 ± 1.8	2.2 ± 1.4	-0.90	0.63
43	9 ^h 12 ^m 09.20 ^s	-65°00'14.31"	3.06"	5.6 ± 0.9	2.5 ± 0.9	-0.28	0.17
44	9 ^h 12 ^m 10.38 ^s	-64°42'45.63"	2.96"	6.6 ± 1.0	1.2 ± 0.6	-0.61	-0.61
45	9 ^h 11 ^m 34.52 ^s	-64°55'58.33"	2.95"	4.6 ± 0.7	0.8 ± 0.4	-0.07	-0.72
46	9 ^h 12 ^m 26.58 ^s	-64°52'57.28"	2.91"	3.6 ± 0.6	0.8 ± 0.4	-0.41	-0.09
47	9 ^h 11 ^m 11.98 ^s	-64°55'04.46"	2.95"	5.4 ± 0.8	1.1 ± 0.6	0.11	-0.74
48	9 ^h 13 ^m 37.18 ^s	-64°59'23.29"	3.01"	9.7 ± 1.6	3.6 ± 1.5	-0.46	0.40
49	9 ^h 10 ^m 43.80 ^s	-64°57'21.68"	3.10"	6.4 ± 1.1	0.9 ± 0.6	-0.43	-0.73
50	9 ^h 12 ^m 39.39 ^s	-64°53'30.91"	3.13"	3.2 ± 0.6	0.6 ± 0.4	-0.74	-0.28
51	9 ^h 11 ^m 19.71 ^s	-65°01'39.27"	3.18"	6.2 ± 1.2	2.0 ± 1.2	0.11	-0.08

Table 2. continued.

ID	RA ₂₀₀₀	Dec ₂₀₀₀	Error	Rate	Flux	HR1	HR2
52	9 ^h 10 ^m 10.14 ^s	-64°49'32.70"	3.36"	9.9 ± 1.9	3.4 ± 1.8	-0.37	0.24
53	9 ^h 11 ^m 27.99 ^s	-64°45'16.78"	3.10"	5.1 ± 1.1	2.5 ± 1.1	-0.15	0.35
54	9 ^h 13 ^m 48.16 ^s	-64°49'13.83"	3.33"	5.8 ± 1.5	1.7 ± 1.1	0.09	-0.44
55	9 ^h 10 ^m 49.56 ^s	-64°53'04.38"	3.01"	4.6 ± 0.8	1.4 ± 0.8	-0.25	-0.34
56	9 ^h 12 ^m 44.02 ^s	-64°57'45.26"	3.17"	4.0 ± 0.8	1.1 ± 0.6	0.04	-0.36
57	9 ^h 11 ^m 31.38 ^s	-64°40'31.48"	3.20"	7.6 ± 1.6	2.8 ± 1.6	-0.10	-0.12
58	9 ^h 10 ^m 06.13 ^s	-64°42'24.11"	3.12"	11.0 ± 2.6	6.0 ± 2.4	-0.50	0.36
59	9 ^h 11 ^m 08.53 ^s	-64°51'13.89"	3.13"	3.3 ± 0.7	1.4 ± 0.6	0.47	-0.27
60	9 ^h 11 ^m 13.27 ^s	-64°44'01.37"	3.22"	6.1 ± 1.2	2.0 ± 1.1	-0.40	0.30
61	9 ^h 11 ^m 54.16 ^s	-65°02'07.50"	3.09"	4.6 ± 1.0	1.9 ± 0.9	0.46	-0.36
62	9 ^h 12 ^m 51.81 ^s	-64°52'10.04"	3.24"	2.6 ± 0.6	0.6 ± 0.5	0.30	-0.41
63	9 ^h 13 ^m 57.26 ^s	-64°49'07.89"	3.30"	3.2 ± 0.8	1.7 ± 1.0	-0.43	-0.50
64	9 ^h 13 ^m 07.10 ^s	-64°38'42.62"	3.86"	8.1 ± 2.2	5.1 ± 2.1	-0.12	0.24
65	9 ^h 14 ^m 07.11 ^s	-64°56'07.10"	3.57"	3.7 ± 0.8	1.4 ± 0.9	-0.77	-0.29
66	9 ^h 11 ^m 37.91 ^s	-64°48'56.44"	3.16"	2.8 ± 0.6	0.7 ± 0.4	-0.81	0.50
67	9 ^h 12 ^m 42.29 ^s	-64°50'33.76"	3.10"	2.3 ± 0.5	1.0 ± 0.5	0.01	-0.30
68	9 ^h 13 ^m 12.00 ^s	-64°49'12.30"	3.28"	3.6 ± 0.8	0.8 ± 0.6	-0.37	-0.02
69	9 ^h 10 ^m 59.37 ^s	-64°47'32.51"	3.20"	3.6 ± 0.9	0.7 ± 0.5	-0.17	-0.66
70	9 ^h 10 ^m 53.55 ^s	-65°01'35.59"	3.12"	6.2 ± 1.4	2.7 ± 1.4	0.09	0.12
71	9 ^h 10 ^m 43.16 ^s	-64°53'13.82"	3.41"	4.1 ± 1.0	1.6 ± 0.8	0.01	0.12
72	9 ^h 12 ^m 46.84 ^s	-65°04'05.62"	3.41"	2.7 ± 0.7	1.1 ± 0.9	-0.62	-0.51
73	9 ^h 13 ^m 25.04 ^s	-64°54'44.82"	3.29"	3.7 ± 0.9	1.0 ± 0.7	-0.21	0.45
74	9 ^h 10 ^m 40.75 ^s	-65°01'06.34"	3.35"	3.4 ± 1.1	0.5 ± 0.8	-0.48	-1.00
75	9 ^h 12 ^m 25.96 ^s	-64°42'14.74"	3.32"	4.4 ± 1.1	1.2 ± 0.8	-0.32	-0.34
76	9 ^h 12 ^m 13.28 ^s	-64°44'30.85"	3.22"	3.3 ± 0.8	2.0 ± 0.9	0.34	0.45
77	9 ^h 12 ^m 23.75 ^s	-64°57'10.31"	3.17"	2.5 ± 0.7	0.9 ± 0.7	-0.38	0.40
78	9 ^h 10 ^m 01.72 ^s	-64°49'35.37"	3.61"	10.1 ± 2.2	4.3 ± 2.1	-0.62	0.76
79	9 ^h 13 ^m 32.54 ^s	-65°01'54.65"	3.23"	4.1 ± 1.0	3.7 ± 1.9	-0.53	0.49
80	9 ^h 13 ^m 25.92 ^s	-64°41'54.45"	3.14"	6.4 ± 1.6	2.3 ± 1.6	-0.37	0.19
81	9 ^h 10 ^m 26.40 ^s	-64°58'32.21"	3.20"	4.5 ± 1.2	1.4 ± 1.1	0.33	-0.15
82	9 ^h 13 ^m 06.79 ^s	-64°46'17.01"	3.30"	3.6 ± 0.9	1.3 ± 0.6	0.18	-0.03
83	9 ^h 10 ^m 39.50 ^s	-64°51'40.97"	3.17"	4.1 ± 1.0	1.9 ± 1.0	-0.06	0.33
84	9 ^h 11 ^m 18.08 ^s	-64°44'05.44"	3.30"	2.7 ± 0.8	0.5 ± 0.6	-1.00	0.33
85	9 ^h 12 ^m 13.60 ^s	-64°47'53.24"	3.07"	2.1 ± 0.5	1.2 ± 0.6	0.40	0.28
86	9 ^h 12 ^m 29.41 ^s	-64°45'58.43"	3.21"	4.1 ± 0.8	2.2 ± 0.9	1.00	0.38
87	9 ^h 13 ^m 03.27 ^s	-64°43'57.14"	3.30"	5.1 ± 1.2	2.6 ± 1.2	0.96	0.24
88	9 ^h 11 ^m 21.58 ^s	-64°56'55.59"	3.13"	2.9 ± 0.7	1.6 ± 0.7	0.67	0.54
89	9 ^h 10 ^m 55.54 ^s	-65°02'46.31"	3.32"	6.2 ± 1.5	2.4 ± 1.4	0.21	0.07
90	9 ^h 14 ^m 02.85 ^s	-64°57'02.65"	3.46"	1.8 ± 0.6	1.6 ± 1.0	-0.45	-0.53
91	9 ^h 12 ^m 30.90 ^s	-64°54'28.17"	3.35"	1.1 ± 0.3	1.2 ± 0.6	0.97	-0.12
92	9 ^h 09 ^m 56.63 ^s	-64°48'46.89"	3.11"	4.7 ± 1.5	0.4 ± 1.0	-0.94	0.00

Table 3. NGC 4372 X-ray source properties. The columns contain the ID of the source, the position (RA₂₀₀₀ and Dec₂₀₀₀) with the error, the rate [$\times 10^{-3}$ count s⁻¹], the flux converted with ECFs in band 0.5–10 keV [$\times 10^{-14}$ erg cm⁻² s⁻¹] and the hardness ratios (*HR*). The *HR* for two energy band *B1* and *B2* are defined by $HR = (B2 - B1)/(B1 + B2)$, *HR1* for 0.5–1.5 and 1.5–3 keV energy bands, *HR2* for 1.5–3 and 3–10 keV energy bands.

ID	RA ₂₀₀₀	Dec ₂₀₀₀	Error	Rate	Flux	<i>HR1</i>	<i>HR2</i>
1	12 ^h 25 ^m 33.82 ^s	-72°27'47.25"	2.74"	221.0 ± 8.4	74.8 ± 9.5	-0.75	-0.72
2	12 ^h 25 ^m 11.18 ^s	-72°27'03.41"	2.74"	250.6 ± 10.1	113.0 ± 15.7	-0.62	-0.44
3	12 ^h 25 ^m 38.57 ^s	-72°49'23.94"	2.81"	38.1 ± 3.3	10.5 ± 4.7	-0.94	-1.00
4	12 ^h 26 ^m 24.22 ^s	-72°32'37.25"	2.89"	27.3 ± 3.2	19.4 ± 6.0	-0.05	-0.37
5	12 ^h 26 ^m 47.98 ^s	-72°42'15.92"	3.02"	15.8 ± 2.3	9.1 ± 4.1	-0.47	-0.28
6	12 ^h 28 ^m 01.38 ^s	-72°43'15.82"	2.92"	19.4 ± 2.5	41.9 ± 7.7	-0.01	0.17
7	12 ^h 28 ^m 09.69 ^s	-72°31'41.34"	3.03"	26.3 ± 3.9	60.1 ± 12.2	0.19	0.14
8	12 ^h 27 ^m 56.17 ^s	-72°41'04.30"	3.03"	13.4 ± 2.2	23.6 ± 6.2	-0.03	-0.07
9	12 ^h 25 ^m 27.76 ^s	-72°26'52.07"	3.69"	21.8 ± 5.5	13.0 ± 11.1	-0.10	-0.55
10	12 ^h 27 ^m 32.84 ^s	-72°40'13.53"	3.32"	5.1 ± 1.3	2.9 ± 2.6	-0.73	-1.00